# Decarbonation Reactions Involving Ankerite and Dolomite under upper Mantle P,T-Parameters: Experimental Modeling

**Yuliya V. Bataleva** [1],* , **Aleksei N. Kruk** [1], **Ivan D. Novoselov** [1,2], **Olga V. Furman** [1,2] **and Yuri N. Palyanov** [1],*

[1] Sobolev Institute of Geology and Mineralogy, Siberian Branch of Russian Academy of Sciences, Koptyug ave 3, 630090 Novosibirsk, Russia; krukan@igm.nsc.ru (A.N.K.); novoselovid@igm.nsc.ru (I.D.N.); furmano@igm.nsc.ru (O.V.F.)

[2] Department of Geology and Geophysics, Novosibirsk State University, Pirogova str 2, 630090 Novosibirsk, Russia

* Correspondence: bataleva@igm.nsc.ru (Y.V.B.); palyanov@igm.nsc.ru (Y.N.P.); Tel.: +7-383-330-75-01 (Y.N.P.)
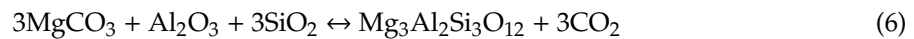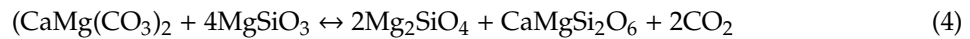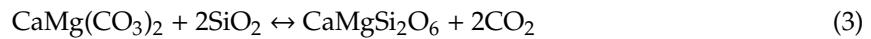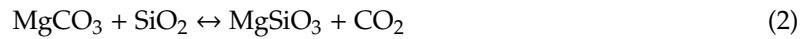
**Abstract:** An experimental study aimed at the modeling of dolomite- and ankerite-involving decarbonation reactions, resulting in the $CO_2$ fluid release and crystallization of Ca, Mg, Fe garnets, was carried out at a wide range of pressures and temperatures of the upper mantle. Experiments were performed using a multi-anvil high-pressure apparatus of a "split-sphere" type, in $CaMg(CO_3)_2$-$Al_2O_3$-$SiO_2$ and $Ca(Mg,Fe)(CO_3)_2$-$Al_2O_3$-$SiO_2$ systems (pressures of 3.0, 6.3 and 7.5 GPa, temperature range of 950–1550 °C, hematite buffered high-pressure cell). It was experimentally shown that decarbonation in the dolomite-bearing system occurred at 1100 ± 20 °C (3.0 GPa), 1320 ± 20 °C (6.3 GPa), and 1450 ± 20 °C (7.5 GPa). As demonstrated by mass spectrometry, the fluid composition was pure $CO_2$. Composition of synthesized garnet was $Prp_{83}Grs_{17}$, with main Raman spectroscopic modes at 368–369, 559–562, and 912–920 $cm^{-1}$. Decarbonation reactions in the ankerite-bearing system were realized at 1000 ± 20 °C (3.0 GPa), 1250 ± 20 °C (6.3 GPa), and 1400 ± 20 °C (7.5 GPa). As a result, the garnet of $Grs_{25}Alm_{40}Prp_{35}$ composition with main Raman peaks at 349–350, 552, and 906–907 $cm^{-1}$ was crystallized. It has been experimentally shown that, in the Earth's mantle, dolomite and ankerite enter decarbonation reactions to form Ca, Mg, Fe garnet + $CO_2$ assemblage at temperatures ~175–500 °C lower than $CaCO_3$ does at constant pressures.

**Keywords:** decarbonation reaction; dolomite; ankerite; garnet; $CO_2$ fluid; experimental modeling; high-pressure experiment

## 1. Introduction

Reconstruction of the global carbon cycle involves studies on natural carbonates and carbides stability, C-O-H fluid generation conditions, modeling of mantle metasomatic processes, and natural diamond formation, as well as the formation and evolution of carbonated rocks. One of the most important planetary-scale settings for studying and understanding the global carbon cycle is subduction. Under subduction conditions, carbon is transported to the Earth's mantle as carbonates and organic material in marine sediments, altered oceanic crust, and basalts [1]. In the course of subduction, carbonates can undergo phase transitions and structure changes (Figure 1a–c) [2,3], partial melting processes (Figure 2) [4–6], decomposition (breakdown) [5–7], dissolution [8,9], or participate various carbonate-consuming reactions. These reactions include diamond-forming redox interactions between carbonates and highly reduced phases [10–12] as well as decarbonation reactions, which lead to the

formation of a $CO_2$ fluid and newly formed silicates/oxides [13–21]. These decarbonation reactions, occurring under mantle P,T-parameters, were experimentally studied in a number of works (Figure 3):

$$MgCO_3 + MgSiO_3 \leftrightarrow Mg_2SiO_4 + CO_2 \tag{1}$$

$$MgCO_3 + SiO_2 \leftrightarrow MgSiO_3 + CO_2 \tag{2}$$

$$CaMg(CO_3)_2 + 2SiO_2 \leftrightarrow CaMgSi_2O_6 + 2CO_2 \tag{3}$$

$$(CaMg(CO_3)_2 + 4MgSiO_3 \leftrightarrow 2Mg_2SiO_4 + CaMgSi_2O_6 + 2CO_2 \tag{4}$$

$$3MgCO_3 + Al_2SiO_5 + 2SiO_2 \leftrightarrow Mg_3Al_2Si_3O_{12} + 3CO_2 \tag{5}$$

$$3MgCO_3 + Al_2O_3 + 3SiO_2 \leftrightarrow Mg_3Al_2Si_3O_{12} + 3CO_2 \tag{6}$$

However, most existing models [22–25] predict that decarbonation, involving Mg and Ca carbonates, occurs at P,T-parameters higher that those supposed for most subduction settings (Figure 3). According to these models, most subducted carbon in the form of Mg,Ca carbonates is transported in the downward moving slab to great depths. The presence of carbonates in the mantle is confirmed by both theoretical and experimental works [6,13–15,17,19,20], as well as numerous findings of carbonate inclusions in diamonds [26–34]. Currently, in most works on experimental modeling of decarbonation reactions involving natural carbonates (1)–(4), the parameters of reaction with the formation of olivine, ortho- and clinopyroxene have been established. Moreover, the position of the decarbonation curves with the formation of garnet was experimentally determined only in the $MgCO_3$-$Al_2O_3$-$SiO_2$ system [20,35] (Figure 4).
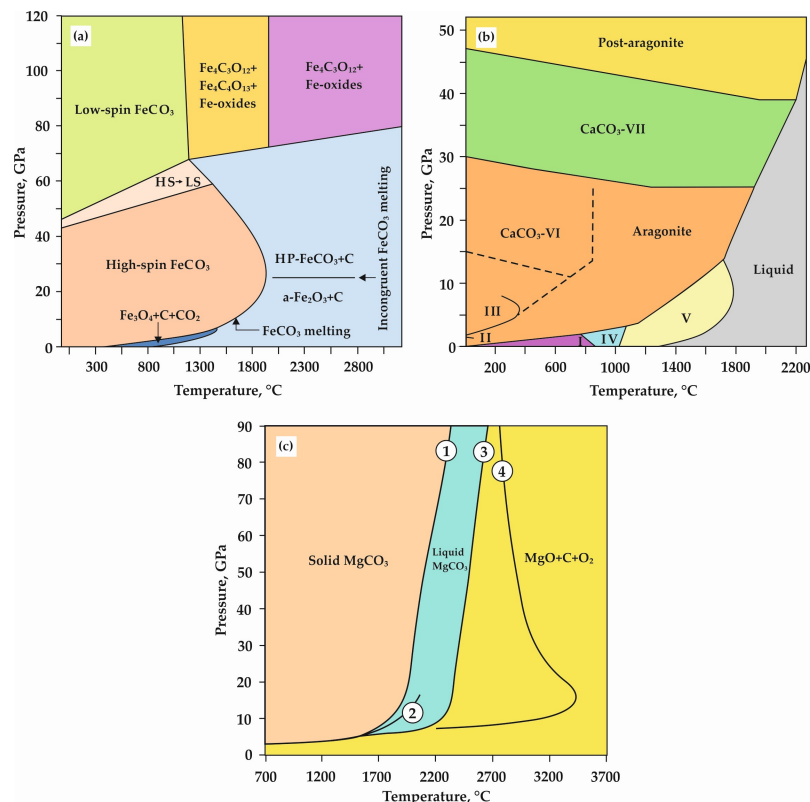


**Figure 1.** Experimentally determined P,T-diagrams of $FeCO_3$ (**a**) (modified from [36–40]), $CaCO_3$ (**b**) (modified from [41,42]) and $MgCO_3$ (**c**) (1—melting curve of $MgCO_3$ [43]; 2—melting curve of $MgCO_3$ [44]; 3—decomposition of liquid $MgCO_3$ into MgO and $CO_2$ [43]; 4—calculated decomposition of $MgCO_3$ [45]. HS—high-spin, LS—low-spin, HP—high-pressure, I,II,III,IV,V—$CaCO_3$ phases.
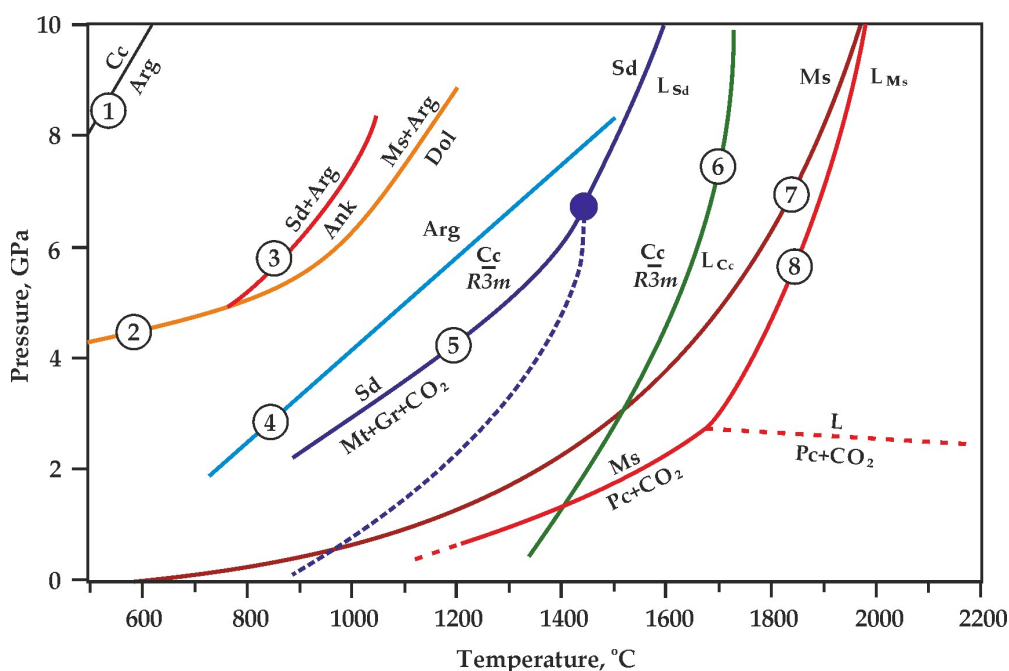
**Figure 2.** Experimentally determined parameters of melting and decomposition of Mg, Ca, Fe carbonates: 1—calcite–aragonite transition [41]; 2—magnesite + aragonite = dolomite [7]; 3—siderite + aragonite = ankerite [7]; 4—aragonite–$CaCO_3$ (R3_m) transition [46]; 5—siderite melting and decomposition [38,39]; 6—$CaCO_3$ melting [47]; 7, 8—magnesite melting and decomposition [6,43]. Sd—siderite, $L_{Sd}$—liquid $FeCO_3$, Mt—magnetite, Gr—graphite, Ms—magnesite, Pc—periclase, $L_{Ms}$—liquid $MgCO_3$, Cc—calcite, Arg—aragonite, Ank—ankerite, LCc—liquid $CaCO_3$.
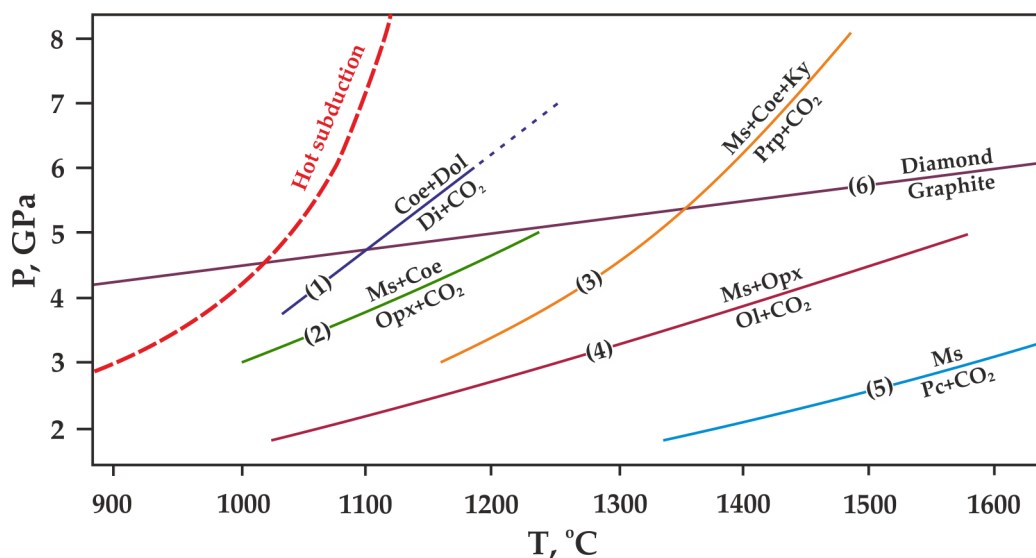


**Figure 3.** P,T diagram with previously constrained decarbonation curves, resulting in the formation of $CO_2$ fluid and (1) diopside [17], (2) orthopyroxene [15,19], (3) pyrope [20], (4) olivine [13,14], (5) periclase [6]. The graphite-diamond direct transition line (6) is given according to [48]. Ms—magnesite, Dol—dolomite, Di—diopside, Pc—periclase, Opx—orthopyroxene (enstatite), Ol—olivine (forsterite), Coe—coesite, Ky—kyanite, Prp—pyrope.
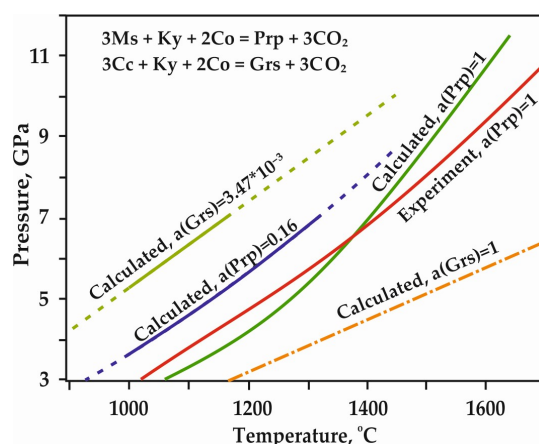
**Figure 4.** P,T diagram with previously experimentally constrained and calculated decarbonation curves, resulting in the formation of $CO_2$ fluid and garnet solid solutions [20]; *a*—activity of component, Ms—magnesite, Ky—kyanite, Co—coesite, Prp—pyrope, Grs—grossular.

Thus, it seems relevant to perform experimental modeling of decarbonation reactions involving natural Mg,Ca carbonates (dolomite, ankerite), and associated with the formation of garnets and $CO_2$ fluid, and to determine the position of the corresponding decarbonation curves at a wide range of pressures and temperatures of the upper mantle.

## 2. Materials and Methods

Experimental modeling of decarbonation reactions involving ankerite and dolomite was performed in the $Ca(Mg,Fe)(CO_3)_2$-$SiO_2$-$Al_2O_3$ and $CaMg(CO_3)_2$-$SiO_2$-$Al_2O_3$ systems using a multi-anvil high-pressure split-sphere apparatus (BARS) [49]. The experiments were carried out at pressures of 3.0, 6.3, and 7.5 GPa, in the temperature range of 950–1550 °C and for durations from 15 min to 60 h. Methodological features of the assembly, the design of the high-pressure cell, as well as data on the pressure and temperature calibration have been published previously [21,50–52]. As initial reagents, we used natural ankerite ($Ca(Mg,Fe)(CO_3)_2$ (Mésage Mine, Saint-Pierre-de-Mésage, France) and dolomite ($CaMg(CO_3)_2$ (Satka, Urals, Russian Federation), as well as synthetic $SiO_2$ and $Al_2O_3$ with a purity of 99.99%. Raman spectra of these natural carbonates are shown in Figure 5. The molar proportions of the starting materials ensure garnet and $CO_2$ fluid formation when the interaction is complete (Table 1). The starting reagents were ground and thoroughly homogenized. Taking into account previous experience of the studies in carbonate-oxide systems under high P and T [53–55], Pt was chosen as the capsule material.
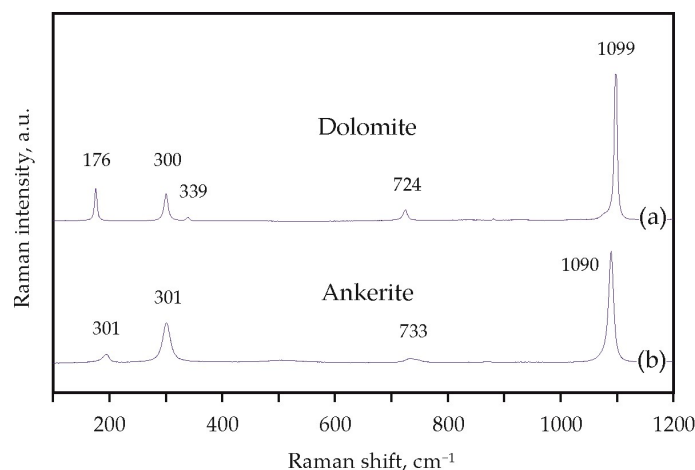


**Figure 5.** Raman spectra of starting materials—natural dolomite (**a**) and ankerite (**b**).

**Table 1.** Weights of initial reagents.

| System | P, GPa | Weight, mg | | |
| --- | --- | --- | --- | --- |
| | | Carbonate | SiO$_2$ | Al$_2$O$_3$ |
| CaMg(CO$_3$)$_2$-SiO$_2$-Al$_2$O$_3$ | 3.0 | 5.0 | 3.2 | 1.8 |
| | 6.3 | 5.0 | 3.2 | 1.8 |
| | 7.5 | 4.0 | 2.6 | 1.4 |
| Ca(Mg,Fe)(CO$_3$)$_2$-SiO$_2$-Al$_2$O$_3$ | 3.0 | 5.2 | 3.1 | 1.8 |
| | 6.3 | 5.2 | 3.1 | 1.8 |
| | 7.5 | 4.1 | 2.5 | 1.4 |

The volume of reaction capsules was selected to ensure that all necessary analytical methods could be employed, taking into account the size of the high-pressure cell. The internal diameter of the Pt capsules for experiments at 3.0 and 6.3 GPa was 1.5 mm at a length of 6 mm, and at 7.5 GPa, 1.5 mm at a length of 4 mm.

There is a problem of hydrogen diffusion into the reaction volume through the walls of capsules in the high-temperature high-pressure experimental studies [56,57]. Hydrogen diffusion can significantly decrease the oxygen fugacity in capsules, change the composition of the fluid in the reaction volume, and lead to a shift in the decarbonation curves in the P,T-field (Figure 6a). To prevent the effect of hydrogen diffusion on the course of the experiment, in this study, we used a specially designed high-pressure cell with a hematite buffer container [51]. The effective time of this buffer at temperatures below 1200 °C is more than 150 h, and at 1500 °C, it is around 5 h. After the experiments, control studies of the chemical composition of the hematite buffer container were carried out. In all cases, the material of the buffer container was analyzed; it was represented by hematite and magnetite, which indicates the effectiveness of the hematite container throughout the entire experiment. The duration of the experiments for each temperature was selected based on the time of effective action of the hematite container. The experimental temperatures were selected according to the calculations (Figure 6b) [58,59].
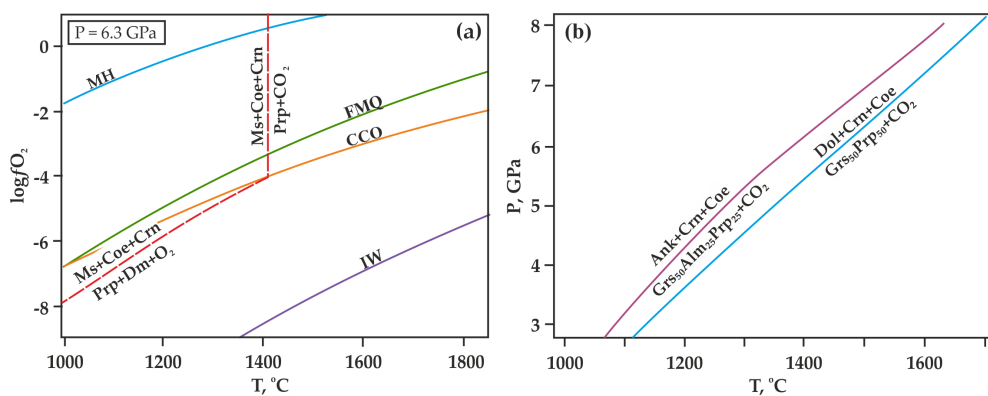


**Figure 6.** T-$f$O$_2$ diagram (**a**) with lines of buffer equilibria (according to [60–62]), as well as the decarbonation reaction [53] and P,T diagram (**b**) with the theoretical positions of decarbonation reactions involving ankerite and dolomite, as calculated in this paper [58,59]. MH (magnetite-hematite), FMQ (fayalite-magnetite-quartz), IW (iron-wüstite), CCO—buffer equilibria; Ms—magnesite, Coe—coesite, Crn—corundum, Prp—pyrope, Mgt—magnetite, Ru—rutile, Ilm—ilmenite, Dm—diamond.

The phase and chemical compositions of the final samples were determined by energy dispersive spectroscopy (Tescan MIRA3 LMU scanning electron microscope, TESCAN, Brno, Czech Republic) and microprobe analysis (Camebax-micro analyzer, CAMECA, Gennevilliers, France). Standards used for the analyses of garnet were pyrope (for SiO$_2$ and Al$_2$O$_3$ contents), ferrous spessartine (for FeO and MnO), and diopside (for MgO and CaO). Silicate, carbonate, and oxide mineral phases were analyzed

at an accelerating voltage of 20 kV, a probe current of 20 nA, a counting time of 10 s on each analytical line, and an electron beam diameter of 2–4 μm. Phase relationships in the samples were studied by means of scanning electron microscopy (SEM).

At the preliminary stage of the experiments, we calculated the theoretical positions of the decarbonation curves (Figure 6b) according to data given in [20] on carbonation curves for grossular, pyrope, and "diluted" grossular. This technique implied ideal mixing for the garnet solid solution. The lines obtained as a result would be true for the complete decarbonation (all ankerite or dolomite is decomposed).

The structural features of the obtained garnet and carbonate were studied by Raman spectroscopy (Jobin Yvon LabRAM HR800 spectrometer equipped with an Olympus BX41 stereo microscope, Horiba Jobin Yvon S.A.S., Lonjumeau, France). An He-Cd laser with a wavelength of 325 nm (Laser Quantum, Stockport, UK) was used as an excitation source. To monitor the effectiveness of the hematite buffer, the composition of the fluid phase was identified by mass spectrometry. For this, the platinum capsule after the experiment was placed in a vacuum device connected to a sample injection system in a Delta V Advantage mass spectrometer (Thermo Fisher Scientific, Bremen, Germany) and equipped with a special mechanism for puncturing samples. After preliminary pumping out of the device with the sample to a pressure of $2.7 \times 10^{-2}$ mbar, guaranteeing the absence of atmospheric gases in the device, the capsule was punctured and the gas released at room temperature was let into the mass spectrometer analyzer. Analytical studies were performed at the Sobolev Institute of Geology and Mineralogy, SB RAS, and at the Analytical Center for multi-elemental and isotope research, SB RAS.

## 3. Results

The experimental parameters and the results obtained are presented in Table 2. Taking into account the previously developed approach [20], the main criterion for the decarbonation reaction to occur is the appearance of garnet and $CO_2$ fluid in the reaction volume. The formation of these phases was accompanied by a decrease in the amount of ankerite or dolomite and oxides in the reaction volume (Figure 7a,b). The partial preservation of carbonate and oxides in the samples is a consequence of the incomplete passage of the decarbonation reaction during the effective time of the hematite buffer.

**Table 2.** Experimental parameters and results.

| Run N | System | P, GPa | T, °C | t, h | Final Mineral Phases |
|---|---|---|---|---|---|
| 1744-A | | 3.0 | 950 | 60 | Ky, Ank, Arg, Coe, Crn |
| 1738-A | | 3.0 | 1050 | 60 | Grt, Ky, Ank, Coe, Crn |
| 2117-A | | 6.3 | 1100 | 40 | Ky, Ank, Coe, Crn |
| 2119-A | | 6.3 | 1200 | 40 | Ky, Ank, Coe, Crn |
| 2115-A | $Ca(Mg,Fe)(CO_3)_2\text{-}SiO_2\text{-}Al_2O_3$ | 6.3 | 1300 | 20 | Grt, Ky, Ank, Coe, Crn |
| 2113-A | | 6.3 | 1400 | 10 | Grt, Ky, Ank, Coe, Crn |
| 2137-A | | 7.5 | 1150 | 60 | Ky, Ank, Coe, Crn |
| 2135-A | | 7.5 | 1250 | 40 | Ky, Ank, Coe, Crn |
| 2141-A | | 7.5 | 1350 | 10 | Ky, Ank, Coe, Crn |
| 2145-A | | 7.5 | 1450 | 10 | Grt, Ky, Ank, Coe, Crn |
| 1743-D | | 3.0 | 1050 | 60 | Ky, Dol, Coe, Crn |
| 2122-D | | 3.0 | 1150 | 60 | Grt, Ky, Dol, Coe, Crn |
| 2160-D | | 6.3 | 1200 | 40 | Ky, Dol, Coe, Crn |
| 2155-D | $CaMg(CO_3)_2\text{-}SiO_2\text{-}Al_2O_3$ | 6.3 | 1250 | 40 | Ky, Dol, Coe, Crn |
| 2128-D | | 6.3 | 1350 | 20 | Grt, Ky, Dol, Coe, Crn |
| 2120-D | | 6.3 | 1450 | 10 | Grt, Ky, Dol, Coe |
| 2161-D | | 7.5 | 1450 | 10 | Ky, Dol, Coe, Crn |
| 2157-D | | 7.5 | 1550 | 15 min | Grt, Coe, Crn |

Grt—garnet, Ank—ankerite, Arg—aragonite, Dol—dolomite, Coe—coesite, Crn—corundum, Ky—kyanite.

At temperatures above the onset of the decarbonation reaction (Figures 7c–f and 8a), grossular–pyrope–almandine and kyanite were formed in the samples. The compositions of the obtained mineral phases are shown in Table 3. The resulting $CO_2$ fluid segregated and formed cavities

in the entire volume of the samples; the size and shape of the cavities depends on the temperature and, accordingly, the depth of the decarbonation reactions. At the initial stage of the system decarbonation, the fluid was in the interstitial space, and with increasing temperature, it formed rounded cavities with sizes from 10 to 150 µm.
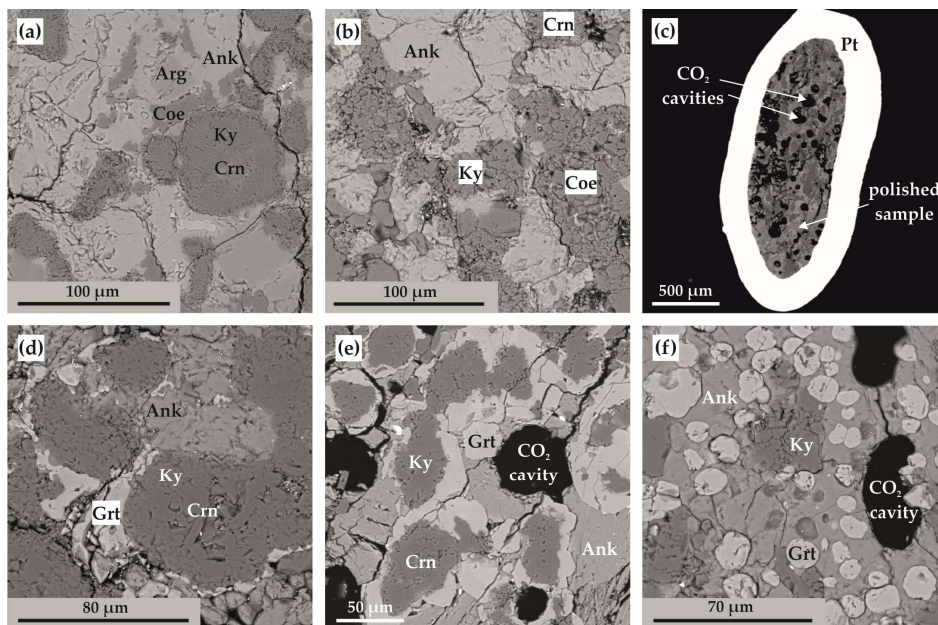


**Figure 7.** SEM micrographs (BSE regime) of polished sample fragments after experiments in $Ca(Mg,Fe)(CO_3)_2$-$SiO_2$-$Al_2O_3$ system: (**a**) polycrystalline aggregate of ankerite, aragonite, coesite, kyanite, and corundum (N 1744-A); (**b**) polycrystalline aggregate of ankerite, coesite, kyanite, and corundum (N 2135-A); (**c**) section of Pt capsule with a sample and fluid cavities therein (N 2113-A); (**d**) zoned aggregates of corundum, kyanite, and garnet in ankerite polycrystalline matrix (run N 1738-A); (**e**) zoned aggregates of corundum, kyanite, and garnet as well as $CO_2$ fluid cavities in ankerite polycrystalline matrix (N 2113-A); (**f**) isometric garnet crystals and $CO_2$ fluid cavities in ankerite-kyanite polycrystalline aggregate (N 2145-A); Ank—ankerite, Arg—aragonite, Coe—coesite, Ky—kyanite, Crn—corundum, Grt—garnet.
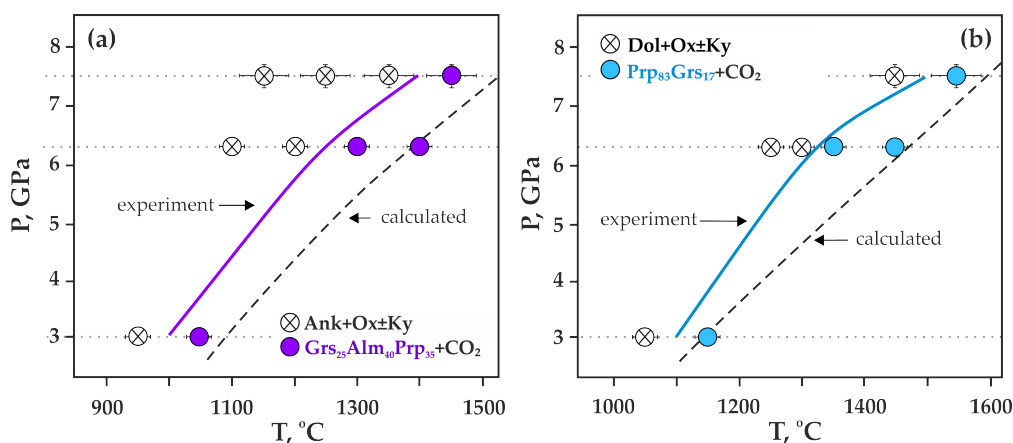


**Figure 8.** P,T diagrams with experimental parameters and results (this study): (**a**) $Ca(Mg,Fe)(CO_3)_2$-$SiO_2$-$Al_2O_3$ system, (**b**) $CaMg(CO_3)_2$-$SiO_2$-$Al_2O_3$ system; dashed lines— calculated position of the reactions of complete decarbonation—$Grs_{50}Prp_{25}Alm_{40}$ (**a**) and $Grs_{50}Prp_{50}$ (**b**).

It was found that decarbonation in the $Ca(Mg,Fe)(CO_3)_2$-$SiO_2$-$Al_2O_3$ system occurred at $1000 \pm 20\,°C$ (3.0 GPa), $1250 \pm 20\,°C$ (6.3 GPa), and $1400 \pm 20\,°C$ (7.5 GPa) (Figure 8a). When studying crystals of synthesized garnet by Raman spectroscopy, it was found that the main modes for them were at $349–350\ cm^{-1}$ (librational $R(SiO_4)^{4-}$), $552\ cm^{-1}$ (internal bending $(Si-O)_{bend}$, $v_2$), and $906–907\ cm^{-1}$ (stretching $(Si-O)_{str}$, $v_1$) (Figure 9a, Table 3). Modes at $403–404, 415, 437, 468, 486, 954\ cm^{-1}$ were noted as secondary modes characteristic of grossular–pyrope–almandine garnet formed as a result of decarbonation reactions. The composition of the obtained garnet in all experiments corresponded to the $Ca_{0.70–0.75}Mg_{0.94–1.15}Fe_{1.10–1.38}Al_{1.92–1.96}Si_3O_{12}$ (Table 4).
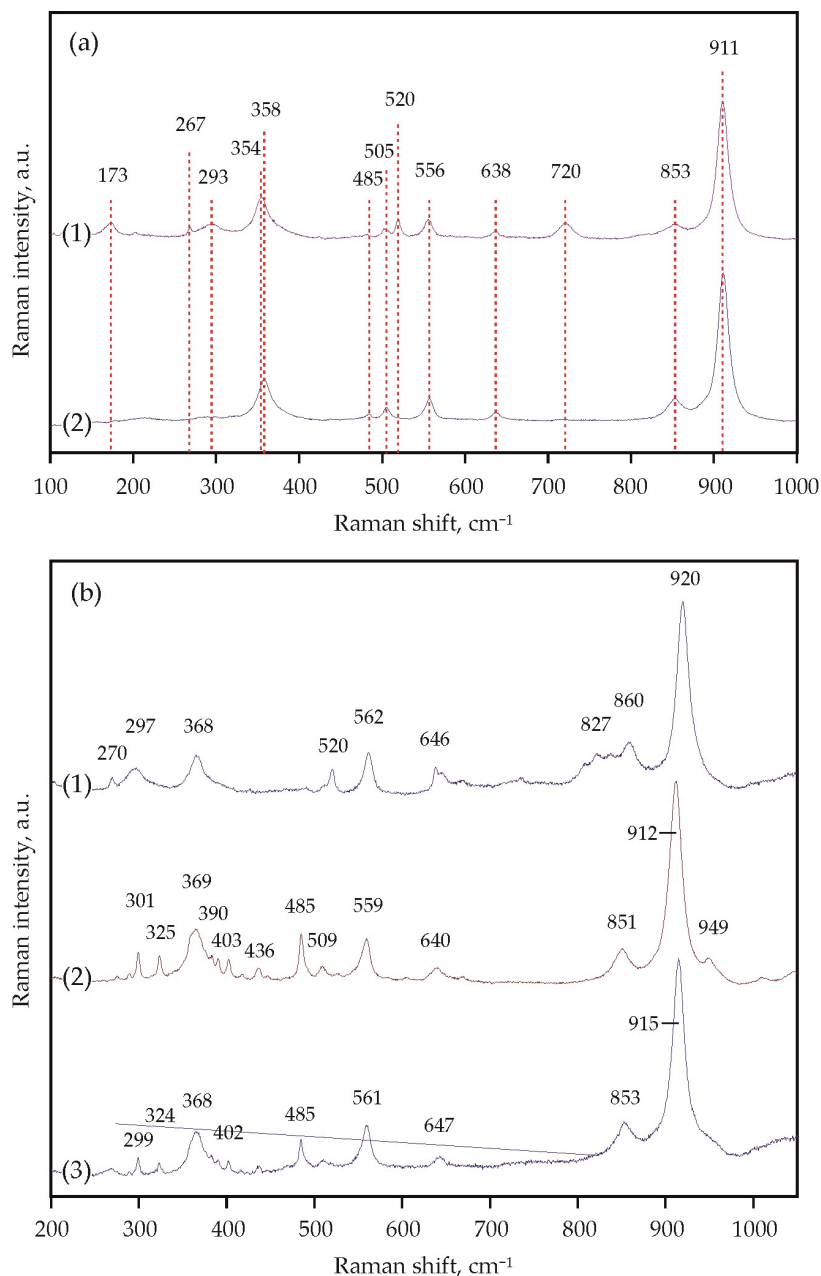


**Figure 9.** Representative Raman spectra of the obtained garnets: (**a**) (1)—run N 2145-A, 7.5 GPa, 1450 °C, (2)—run N 2115-A, 6.3 GPa, 1300 °C; (**b**) (1)—run N 2157-D, 7.5 GPa, 1550 °C, (2)—run N 2155-D, 6.3 GPa, 1250 °C, (3)—run N 2122-D, 3.0 GPa, 1150 °C.

**Table 3.** Raman characterization of synthesized garnets.

| Run N | 2115-A | 2145-A | 2122-D | 2155-D | 2157-D |
|---|---|---|---|---|---|
| Phase | $Alm_{36}Pp_{38}Grs_{26}$ | $Alm_{43}Prp_{34}Grs_{23}$ | $Pp_{74}Grs_{26}$ | $Pp_{70}Grs_{30}$ | $Prp_{84}Grs_{16}$ |
| **Raman Shift, cm$^{-1}$** | | | | | |
| $R(SiO_4)^{4-}$ | - | 173 | - | - | - |
| | - | 267 | - | - | 270 |
| | - | 293 | 299 | 301 | 297 |
| | - | - | 324 | 325 | - |
| | 358 | 354 | 368 | 369 | 368 |
| | - | - | - | 390 | - |
| | - | - | 402 | 403 | - |
| | - | - | - | 436 | - |
| | 485 | - | 485 | 485 | - |
| | 505 | 505 | - | 509 | - |
| | - | 520 | - | - | 520 |
| $(Si-O)_{bend}, \upsilon_2$ | 557 | 556 | 561 | 559 | 562 |
| | 638 | 638 | 647 | 640 | 646 |
| | - | 720 | - | - | - |
| | - | - | - | - | 827 |
| | 853 | 853 | 853 | 851 | 860 |
| $(Si-O)_{str}, \upsilon_1$ | 911 | 911 | 915 | 912 | 920 |
| | - | - | - | 949 | - |

Prp—pyrope, Alm—almandine, Grs—grossular.

**Table 4.** Averaged compositions of garnets, kyanite, and carbonates after experiments in $Ca(Mg,Fe)(CO_3)_2$-$SiO_2$-$Al_2O_3$ system.

| Run N | P, GPa | T, °C | Phase | Mass Concentrations, wt. % | | | | | | | |
|---|---|---|---|---|---|---|---|---|---|---|---|
| | | | | $SiO_2$ | $Al_2O_3$ | FeO | MnO | MgO | CaO | $CO_2$ * | Total |
| 1744-A | 950 | 3.0 | Ky | $34_{(1)}$ | $66.1_{(4)}$ | $0.6_{(1)}$ | - | - | - | - | 100.5 |
| | | | Ank | - | - | $17_{(3)}$ | $0.5_{(1)}$ | $9_{(1)}$ | $28_{(4)}$ | $45_{(1)}$ | 100.0 |
| 1738-A | 1050 | 3.0 | Grt | $39.3_{(3)}$ | $21.8_{(1)}$ | $21.7_{(5)}$ | $0.5_{(0)}$ | $7.3_{(5)}$ | $9.0_{(3)}$ | - | 100.5 |
| | | | Ky | $34.5_{(4)}$ | $64_{(1)}$ | $0.9_{(1)}$ | - | - | - | - | 99.3 |
| | | | Ank | - | - | $15_{(2)}$ | $0.4_{(1)}$ | $12.8_{(4)}$ | $28_{(2)}$ | $43.9_{(7)}$ | 100.0 |
| 2117-A | 1100 | 6.3 | Ky | $35.8_{(8)}$ | $63.6_{(7)}$ | $0.5_{(1)}$ | - | - | - | - | 100.0 |
| | | | Ank | - | - | $13.4_{(4)}$ | $0.5_{(0)}$ | $9.6_{(3)}$ | $32.6_{(4)}$ | $44.0_{(4)}$ | 100.0 |
| 2119-A | 1200 | 6.3 | Ky | $35.6_{(3)}$ | $64.1_{(9)}$ | $1.0_{(0)}$ | - | - | - | - | 100.3 |
| | | | Ank | - | - | $17.8_{(9)}$ | $0.6_{(1)}$ | $10_{(1)}$ | $28_{(1)}$ | $45_{(1)}$ | 100.0 |
| 2115-A | 1300 | 6.3 | Grt | $39.9_{(4)}$ | $22.0_{(5)}$ | $18_{(3)}$ | $0.6_{(1)}$ | $10.3_{(9)}$ | $9_{(1)}$ | - | 100.2 |
| | | | Ank | - | - | $14.9_{(1)}$ | - | $8.4_{(2)}$ | $30.2_{(1)}$ | $46.3_{(3)}$ | 100.0 |
| | | | Ky | $35.5_{(7)}$ | $64_{(1)}$ | $1.0_{(1)}$ | - | - | - | - | 100.3 |
| 2113-A | 1400 | 6.3 | Grt | $39.4_{(5)}$ | $21.4_{(5)}$ | $20_{(1)}$ | $0.7_{(0)}$ | $10.1_{(3)}$ | $9_{(1)}$ | - | 99.7 |
| | | | Ank | - | - | $18_{(2)}$ | $0.3_{(0)}$ | $7.2_{(8)}$ | $29.2_{(7)}$ | $45.3_{(6)}$ | 100.0 |
| | | | Ky | $36_{(1)}$ | $62_{(1)}$ | $2.0_{(2)}$ | - | - | - | - | 99.8 |
| 2137-A | 1150 | 7.5 | Ky | $36.5_{(4)}$ | $62.9_{(4)}$ | $0.7_{(2)}$ | - | - | - | - | 100.2 |
| | | | Ank | - | - | $19_{(1)}$ | $0.5_{(1)}$ | $11_{(1)}$ | $26_{(2)}$ | $43.4_{(8)}$ | 100.0 |
| 2135-A | 1250 | 7.5 | Ky | $36.1_{(1)}$ | $62.4_{(3)}$ | $0.5_{(9)}$ | - | - | $0.4_{(2)}$ | - | 99.6 |
| | | | Ank | - | $0.2_{(0)}$ | $15_{(2)}$ | $0.5_{(1)}$ | $12_{(2)}$ | $28_{(3)}$ | $44.9_{(8)}$ | 100.0 |
| 2141-A | 1350 | 7.5 | Ky | $36.1_{(2)}$ | $62.9_{(5)}$ | $1.7_{(2)}$ | - | - | - | - | 99.5 |
| | | | Ank | - | - | $17_{(1)}$ | $0.5_{(1)}$ | $11.2_{(6)}$ | $26.1_{(8)}$ | $45.3_{(9)}$ | 100.0 |
| 2145-A | 1450 | 7.5 | Grt | $39.5_{(4)}$ | $21.7_{(1)}$ | $20.8_{(5)}$ | $0.7_{(0)}$ | $9.1_{(7)}$ | $8.6_{(5)}$ | - | 100.4 |
| | | | Ky | $35.3_{(3)}$ | $62.5_{(7)}$ | $1.7_{(4)}$ | - | - | $0.2_{(3)}$ | - | 99.6 |
| | | | Ank | - | - | $13.5_{(4)}$ | $0.5_{(1)}$ | $13.0_{(6)}$ | $28_{(1)}$ | $44.6_{(6)}$ | 100.0 |

Ank—ankerite, Coe—coesite, Ky—kyanite, Crn—corundum, Grt—garnet; *—calculated after the sum deficit; the values in parentheses are one sigma errors of the means based on replicate electron microprobe analyses reported as least units cited; 36.1 $_{(1)}$ should be read as 36.1 ± 0.1 wt. %.

In a dolomite-bearing system ($CaMg(CO_3)_2$-$SiO_2$-$Al_2O_3$), experiments were carried out in the temperature ranges of 1050–1150 °C (3.0 GPa), 1150–1450 °C (6.3 GPa), and 1450–1550 °C (7.5 GPa). Recrystallization of the initial dolomite and oxides, as well as a small amount of newly formed kyanite at

the contacts of corundum and coesite (Figure 10a), was established in samples obtained at temperatures below the decarbonation reactions. At higher temperatures, after the onset of the decarbonation reaction (Figure 10b–f), grossular–pyrope garnet and $CO_2$ fluid, kyanite, and recrystallized carbonates and oxides are formed. During the experiments, the resulting fluid segregated and formed cavities in the samples (from 50 to 100 μm) (Figure 10c,f). The compositions of the obtained mineral phases are shown in Table 5. The composition of synthesized garnet in all experiments corresponded to $Ca_{0.5–0.8}Mg_{2.23–2.57}Al_{1.92–1.98}Si_3O_{12}$.

It was found that decarbonation in the $CaMg(CO_3)_2$-$SiO_2$-$Al_2O_3$ system occurs at 1100 ± 20 °C (3.0 GPa), 1320 ± 20 °C (6.3 GPa), and 1450 ± 20 °C (7.5 GPa) (Figure 8b). The main Raman characteristics of the obtained garnet are peaks at 368–369 $cm^{-1}$ ($R(SiO_4)^{4-}$), 559–562 $cm^{-1}$ (($Si$-$O$)$_{bend}$, $\nu_2$), and 912–920 $cm^{-1}$ (($Si$-$O$)$_{str}$, $\nu_1$) (Figure 9b, Table 3), and peaks at 270, 297–301, 402–403, 485, 520, 640–647, 851–860 $cm^{-1}$ are noted as secondary modes. In most experiments, fluid composition was monitored by mass spectrometry. At temperatures below decarbonation, no fluid was found in samples. At temperatures above decarbonation onset, scanning the mass range from 12 to 46 amu revealed the presence of peaks at masses 44, 45, and 46, which correspond exclusively to $CO_2$ (at other masses, the signals did not exceed the background values). It was established that in both relatively low- and high-temperature experiments, the fluid composition corresponded to pure $CO_2$, without impurities of hydrogen or water. The obtained results of mass spectrometry are the best evidence of the effective operation of the hematite buffer and, accordingly, adequate experimental results.
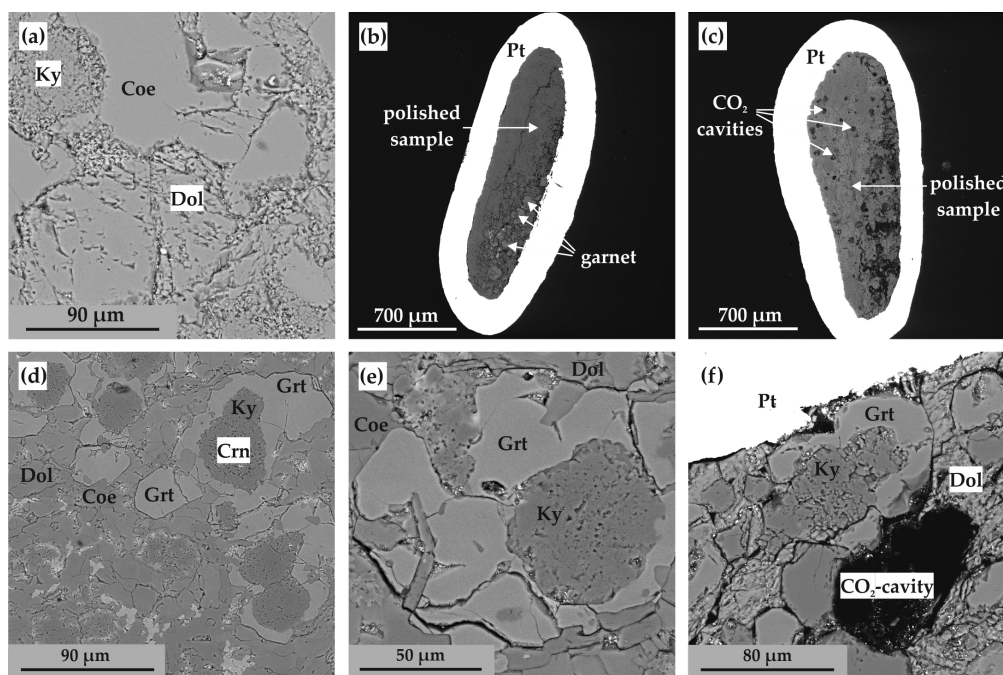


**Figure 10.** SEM micrographs (backscattered electrons (BSE) regime) of polished sample fragments ($CaMg(CO_3)_2$-$SiO_2$-$Al_2O_3$ system): (**a**) polycrystalline aggregate of dolomite, coesite and kyanite (N 1743-D); (**b,c**) sections of Pt-capsules with samples (N 2155-D and 2157-D); (**d,e**) zoned aggregates of corundum, kyanite, and garnet in dolomite–coesite polycrystalline matrix (N 2122-D and 2112-D); (**f**) zoned aggregates of kyanite and garnet and $CO_2$ fluid cavities in dolomite–coesite polycrystalline matrix (N 2120-D); Dol—dolomite, Coe—coesite, Ky—kyanite, Crn—corundum, Grt—garnet.

**Table 5.** Averaged compositions of garnets, kyanite, and carbonates after experiments in $CaMg(CO_3)_2$-$SiO_2$-$Al_2O_3$ system.

| Run N | P, GPa | T, °C | Phase | Mass Concentrations, wt. % | | | | | |
|---|---|---|---|---|---|---|---|---|---|
| | | | | $SiO_2$ | $Al_2O_3$ | MgO | CaO | $CO_2$ | Total |
| 1743-D | 3.0 | 1050 | Ky | 36.0$_{(1)}$ | 64.2$_{(6)}$ | - | - | - | 100.2 |
| | | | Dol | - | - | 21.6$_{(8)}$ | 29.8$_{(4)}$ | 48.6$_{(9)}$ | 100.0 |
| 2122-D | 3.0 | 1150 | Grt | 43.3$_{(3)}$ | 24.2$_{(1)}$ | 21.6$_{(4)}$ | 10.7$_{(8)}$ | - | 99.7 |
| | | | Ky | 33$_{(2)}$ | 67$_{(2)}$ | - | - | - | 100.1 |
| | | | Dol | - | - | 18$_{(1)}$ | 34$_{(1)}$ | 47.7$_{(5)}$ | 100.0 |
| 2160-D | 6.3 | 1200 | Ky | 36.2$_{(3)}$ | 63.8$_{(7)}$ | - | - | - | 100.1 |
| | | | Dol | - | - | 25.3$_{(5)}$ | 24.9$_{(5)}$ | 49.8$_{(4)}$ | 100.0 |
| 2155-D | 6.3 | 1250 | Ky | 35.3$_{(6)}$ | 64.8$_{(5)}$ | - | - | - | 100.1 |
| | | | Dol | - | - | 20.7$_{(8)}$ | 30.4$_{(9)}$ | 48.9$_{(3)}$ | 100.0 |
| 2128-D | 6.3 | 1350 | Grt | 43.3$_{(3)}$ | 24.3$_{(1)}$ | 22.8$_{(3)}$ | 9.1$_{(3)}$ | - | 99.5 |
| | | | Ky | 36.7$_{(1)}$ | 62.5$_{(2)}$ | - | - | - | 99.1 |
| | | | Dol | - | - | 26.2$_{(6)}$ | 24.6$_{(0)}$ | 49.0$_{(4)}$ | 100.0 |
| 2120-D | 6.3 | 1450 | Grt | 44.1$_{(3)}$ | 22.9$_{(3)}$ | 23.2$_{(2)}$ | 9.3$_{(4)}$ | - | 100.6 |
| | | | Ky | 34.1$_{(4)}$ | 66.2$_{(4)}$ | - | - | - | 100.3 |
| | | | Dol | - | - | 16.3$_{(8)}$ | 38.7$_{(7)}$ | 45.0$_{(3)}$ | 100.0 |
| 2161-D | 7.5 | 1450 | Ky | 36.5$_{(5)}$ | 63.6$_{(4)}$ | - | - | - | 100.1 |
| | | | Dol | - | - | 25.2$_{(4)}$ | 25.6$_{(0)}$ | 49.2$_{(3)}$ | 100.0 |
| 2157-D | 7.5 | 1550 | Grt | 42.1$_{(3)}$ | 23.5$_{(1)}$ | 21.5$_{(2)}$ | 11.5$_{(5)}$ | - | 99.5 |
| | | | Ky | 33.7$_{(2)}$ | 66.5$_{(0)}$ | - | - | - | 100.2 |
| | | | Dol | - | - | 19.8$_{(1)}$ | 31.7$_{(2)}$ | 48.5$_{(5)}$ | 100.0 |

Grt—garnet, Dol—dolomite, Ky—kyanite; the values in parentheses are one sigma errors of the means based on replicate electron microprobe analyses reported as least units cited; 6.1 $_{(1)}$ should be read as 6.1 ± 0.1 wt. %.

## 4. Discussion

A detailed study of the phase and chemical composition of the obtained samples, as well as the characteristic structures of the zonal aggregates, makes it possible to reconstruct decarbonation processes in the carbonate–oxide systems $CaMg(CO_3)_2$-$Al_2O_3$-$SiO_2$ and $Ca(Mg,Fe)(CO_3)_2$-$Al_2O_3$-$SiO_2$. It was experimentally demonstrated that at temperatures below the onset of decarbonation reactions in the reaction volume, an interaction between coesite and corundum occurs, with the formation of kyanite at the contact of these phases. A similar process was previously established in the carbonate–oxide–sulfide system ($MgCO_3$–$SiO_2$–$Al_2O_3$–FeS system, P = 6.3 GPa, T = 1250–1450 °C) [11]. At the same time, it must be emphasized that both ankerite and dolomite under P,T parameters below the decarbonation reactions in the samples are stable and do not undergo breakdown or phase transitions, which is confirmed by the results of Raman spectroscopy and mass spectrometry and is also consistent with modern experimental data (Figure 2) [7].

At temperatures above the onset of decarbonation, a number of processes occur in the reaction volume: (1) crystallization of kyanite, (2) interactions of kyanite + coesite + carbonate and corundum + coesite + carbonate, leading to crystallization of garnet and $CO_2$ fluid release, and (3) recrystallization of the starting carbonates and change of their compositions. It was established that the proportions of Ca, Mg, and Fe in the synthesized garnets differ from the initial carbonates. It should be noted that the methodical approach with hematite buffer limits the duration of the experiments; therefore, only partial rather than complete decarbonation is realized in the samples. In the case of complete decarbonation, the molar ratio of divalent cations in the initial carbonate and newly formed garnet would be completely identical. However, it is the established features of partially realized decarbonation reactions that make it possible to reconstruct natural processes. The main regularities were as follows: a decrease in Ca# and an increase in Fe# in garnets relative to the proportions in the initial carbonates; a corresponding increase in Ca# and a decrease in Fe# in carbonates after the experiments, relative to the initial ones (Figure 11).
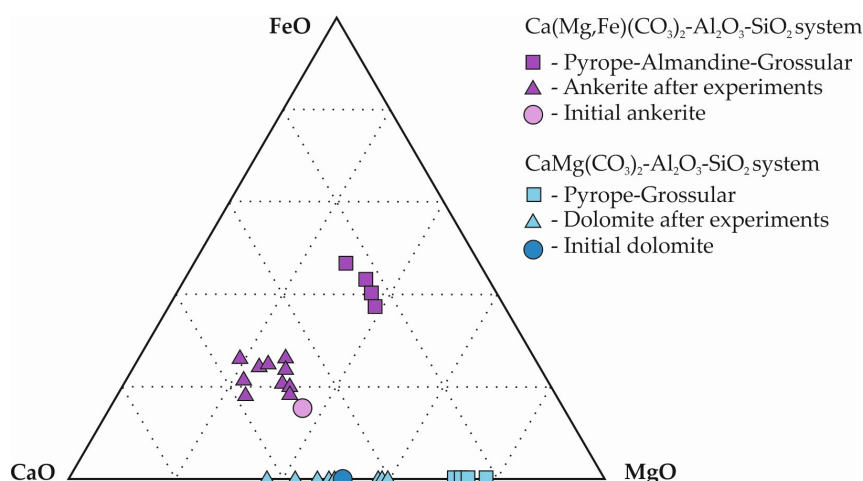
**Figure 11.** Triangle diagram of the averaged chemical compositions (mol.%) of garnets and carbonates.

According to the existing theoretical and experimental data on the decarbonation parameters of Fe, Ca, Mg carbonate–oxide systems, the lowest temperatures are required for the formation of ferrous garnets and the highest for calcium ones [20,58,59]. Specifically, it was demonstrated that diluting pyrope with the almandine component causes temperature downshift of decarbonation reactions, while adding a grossular component, on the contrary, increases the reaction temperature (Figure 4). Correspondingly, $CO_2$ fluid and garnets with decreased Ca# and increased Fe# obtained in this work as a result of partial decarbonation of dolomite or ankerite-bearing assemblages are formed at temperatures lower than those necessary for complete decarbonation. This process is accompanied by a specific change in the composition of dolomite or ankerite (an increase in Ca# and a decrease in Fe# relative to the initial ones), expanding the stability field of these carbonates without significantly changing their structures.

Despite the fact that, in the present study, we performed experiments on the elucidating of positions of decarbonation curves in dry systems, we find it useful to discuss the principal differences between our results and existing ideas on realistic mantle conditions where aqueous fluids are present. In our previous research [16,21] on the formation of diamond and graphite via the carbonate–silicate interaction in $MgCO_3$-$SiO_2$, $CaMg(CO_3)_2$-$SiO_2$ and $MgCO_3$-$SiO_2$-$Al_2O_3$ systems under mantle P,T conditions, the source of hydrogen was used. According to gas chromatographic data, fluid composition during diamond crystallization varied from almost pure $CO_2$ to aqueous, and it strongly affected the decarbonation parameters. For example, in the $MgCO_3$-$SiO_2$ system at 1500 °C and 6 GPa, in the case of $H_2O$-$CO_2$ fluid presence in the reaction volume, the formation of enstatite was recorded, i.e., decarbonation occurred; with the same parameters but in a "dry" system, the final assemblage was magnesite and coesite, i.e., no decarbonation processes took place. In the $MgCO_3$-$Al_2O_3$-$SiO_2$ system at 6 GPa and 1500 °C, the formation of garnet occurred regardless of the fluid composition. However, when $H_2O$-component dominated in fluid, the amount of pyrope increases sharply, which can be explained both by the additional decomposition of magnesite, not only due to the thermodynamic factor but also due to the redox factor, and by an increase in kinetics due to the formation of an aqueous fluid. Another important result obtained is evidence of poor wettability of carbon dioxide under mantle P,T parameters, obtained from the specific structural features of experimental samples. As shown in Figure 7c,e,f and Figure 10c,f, fluid segregates and forms rounded bubbles, which allows us to determine the high wetting angle; this is in good agreement with studies of $CO_2$ fluid wetting properties under crustal conditions [63,64]. Thus, implicating the results both of our present and previous [16,21] studies on the mantle processes, we can state that the presence of water-bearing fluids will reduce the temperatures of garnet + $CO_2$ fluid formation and overall increase the intensity of the decarbonation process. The formation of $H_2O$-$CO_2$ fluid under these conditions results in the better wettability of mantle rocks with fluid, its better migration, and wider distribution of this mantle metasomatic agent.

As a natural media simulated in this paper, one can consider carbonated eclogite. The stability field of garnet + clinopyroxene + kyanite + coesite + carbonate assemblage relatively to garnet + clinopyroxene + $CO_2$ depends on garnet and clinopyroxene carbonation/decarbonation P,T parameters. Processes of carbonation/decarbonation also influence the mantle fluid regime and global cycle of carbon. Results obtained in the present study show that an increase in the Ca component of carbonate expands its stability field, while increasing the Fe component has the opposite effect, or, in other words, Fe-rich garnets have a larger stability field than Ca-rich ones. Thus, it can be suggested that the association of group I eclogites is more stable in processes of $CO_2$ metasomatism than that of group II, as group I garnets are richer in iron and lower in calcium [65]. Carbonation of garnet, however, occurs under higher pressures than that of pyroxenes (reactions (2–4)), which should be taken into account (Knoche et al., 1999) [20]. Another important aspect of this work is the use of a hematite buffer. This allows us to study a non-ultrareduced dry system and observe the decarbonation reaction without formation of carbonatite-like melts, leaving, however, a possibility for further research into water-bearing systems.

The currently available information on inclusions of Ca, Mg, Fe carbonates in natural diamonds, as well as on the composition of garnets from carbonated eclogites, indicates that the data obtained in this work can be fully applicable in the reconstruction of decarbonation processes in the Earth's mantle. In particular, diamonds of pipes of Mwadui, Tansania [31], Juina, Brasil [66], and Cancan, Guinea [67] contain dolomite inclusions (Ca# ~0.5) and siderite (63.5 wt. % FeO). Ankerite microinclusions are also described in a number of works [68,69]. The composition of garnets from eclogite xenoliths varies over a wide range of Mg# 0.46–0.89, Ca# 0.02–0.42, with an average content of Fe# 0.30 [66,70]. Thus, the results of the present experimental study on the estimation of $CO_2$ and double carbonates' stability fields in the Earth's mantle can be used in terms of constraints of diamond-forming processes, with a $CO_2$ as a carbon source for diamond crystallization [71–73].

When comparing the obtained data on the position of decarbonation curves with experimental and calculated results [20], it was found that decarbonation of the $CaMg(CO_3)_2$-$Al_2O_3$-$SiO_2$ (Ca# 49) system begins at 170 °C (3.0 GPa), 330 °C (6.3 GPa), and 400 °C (7.5 GPa) lower than $CaCO_3$-$Al_2O_3$-$SiO_2$ and 100 °C (3.0 GPa) and 50 °C (6.3 GPa) higher than $MgCO_3$-$Al_2O_3$-$SiO_2$. When comparing the positions of decarbonation curves with the participation of ankerite and dolomite obtained in this work, it was demonstrated that the formation of garnet in the system with ankerite occurs at temperatures of 100 °C (3.0 GPa), 70 °C (6.3 GPa), and 50 °C (7.5 GPa) lower than in a system with dolomite.

## References

1. Evans, K.A. The redox budget of subduction zones. *Earth Sci. Rev.* **2012**, *113*, 11–32. [CrossRef]
2. Luth, R.W. Carbon and carbonates in mantle. In *Mantle Petrology: Field Observation and High Pressure Experimentation: A Tribute to Francis, R. (Joe) Boyd*; Fei, Y., Bertka, M.C., Mysen, B.O., Eds.; The Geochemical Society: Washington, DC, USA, 1999; pp. 297–316. ISBN 0-941809-05-6.
3. Stagno, V. Carbon, carbides, carbonates and carbonatitic melts in the Earth's interior. *J. Geol. Soc.* **2019**, *176*, 375–387. [CrossRef]

4.　Dasgupta, R.; Hirschmann, M.M. The deep carbon cycle and melting in Earth's interior. *Earth Planet. Sci. Lett.* **2010**, *298*, 1–13. [CrossRef]

5.　Jones, A.; Genge, M.; Carmody, L. Carbonate melts and carbonatites. *Rev. Miner. Geochem.* **2013**, *75*, 289–322. [CrossRef]

6.　Shatskiy, A.F.; Litasov, K.D.; Palyanov, Y.N. Phase relations in carbonate systems at pressures and temperatures of lithospheric mantle: Review of experimental data. *Russ. Geol. Geophys.* **2015**, *56*, 113–142. [CrossRef]

7.　Morlidge, M.; Pawley, A.; Droop, G. Double carbonate breakdown reactions at high pressures: An experimental study in the system CaO-MgO-FeO-MnO-$CO_2$. *Contrib. Miner. Pet.* **2006**, *152*, 365–373. [CrossRef]

8.　Frezzotti, M.L.; Selverstone, J.; Sharp, Z.D.; Compagnoni, R. Carbonate dissolution during subduction revealed by diamond-bearing rocks from the Alps. *Nat. Geosci.* **2011**, *4*, 703–706. [CrossRef]

9.　Kelemen, P.B.; Manning, C.E. Reevaluating carbon fluxes in subduction zones. *Proc. Natl. Acad. Sci. USA* **2015**, *112*, E3997–E4006. [CrossRef]

10.　Gunn, S.C.; Luth, R.W. Carbonate reduction by Fe–S–O melts at high pressure and high temperature. *Am. Miner.* **2006**, *91*, 1110–1116. [CrossRef]

11.　Palyanov, Y.N.; Borzdov, Y.M.; Bataleva, Y.V.; Sokol, A.G.; Palyanova, G.A.; Kupriyanov, I.N. Reducing role of sulfides and diamond formation in the Earth's mantle. *Earth Planet. Sci. Lett.* **2007**, *260*, 242–256. [CrossRef]

12.　Bataleva, Y.V.; Palyanov, Y.N.; Sokol, A.G.; Borzdov, Y.M.; Bayukov, O.A. Wüstite stability in the presence of a $CO_2$-fluid and a carbonate-silicate melt: Implications for the graphite/diamond formation and generation of Fe-rich mantle metasomatic agents. *Lithos* **2016**, *244*, 20–29. [CrossRef]

13.　Newton, R.C.; Sharp, W.E. Stability of forsterite + $CO_2$ and its bearing on the role of $CO_2$ in the mantle. *Earth Planet. Sci. Lett.* **1975**, *26*, 239–244. [CrossRef]

14.　Koziol, A.M.; Newton, R.C. Experimental determination of the reaction: Magnesite + enstatite = forsterite + $CO_2$ in the ranges 6–25 kbar and 700–1100 °C. *Am. Min.* **1998**, *83*, 213–219. [CrossRef]

15.　Wyllie, P.J.; Huang, W.-L.; Otto, J.; Byrnes, A.P. Carbonation of peridotites and decarbonation of siliceous dolomites represented in the system CaO-MgO-$SiO_2$-$CO_2$ to 30 kbar. *Tectonophys.* **1983**, *100*, 359–388. [CrossRef]

16.　Pal'yanov, Y.N.; Sokol, A.G.; Tomilenko, A.A.; Sobolev, N.V. Conditions of diamond formation through carbonate-silicate interaction. *Eur. J. Miner.* **2005**, *17*, 207–214. [CrossRef]

17.　Luth, R.W. Experimental determination of the reaction dolomite + 2 coesite = diopside + 2 $CO_2$ to 6 GPa. *Contrib. Miner. Pet.* **1995**, *122*, 152–158. [CrossRef]

18.　Wyllie, P.J. Magmas and volatile components. *Am. Miner.* **1979**, *64*, 469–500.

19.　Eggler, D.H. The effect of $CO_2$ upon partial melting of peridotite in the system $Na_2O$-CaO-$Al_2O_3$-MgO-$SiO_2$-$CO_2$ to 35 kbar, with an analysis of melting in a peridotite-$H_2O$-$CO_2$ system. *Am. J. Sci.* **1978**, *278*, 305–343. [CrossRef]

20.　Knoche, R.; Sweeney, R.J.; Luth, R.W. Carbonation and decarbonation of eclogites: The role of garnet. *Contrib. Miner. Pet.* **1999**, *135*, 332–339. [CrossRef]

21.　Pal'yanov, Y.N.; Sokol, A.G.; Borzdov, Y.M.; Khokhryakov, A.F.; Sobolev, N.V. Diamond formation through carbonate-silicate interaction. *Am. Miner.* **2002**, *87*, 1009–1013. [CrossRef]

22.　Connolly, J.A.D. Computation of phase equilibria by linear programming: A tool for geodynamic modeling and its application to subduction zone decarbonation. *Earth Planet. Sci. Lett.* **2005**, *236*, 524–541. [CrossRef]

23.　Gorman, P.J.; Kerrick, D.M.; Connolly, J.A.D. Modeling open system metamorphic decarbonation of subducting slabs. *Geochem. Geophys. Geosyst.* **2006**, *7*, Q04007. [CrossRef]

24.　Molina, J.F.; Poli, S. Carbonate stability and fluid composition in subducted oceanic crust: An experimental study on $H_2O$-$CO_2$-bearing basalts. *Earth Planet. Sci. Lett.* **2000**, *176*, 295–310. [CrossRef]

25.　Poli, S.; Franzolin, E.; Fumagalli, P.; Crottini, A. The transport of carbon and hydrogen in subducted oceanic crust: An experimental study to 5 GPa. *Earth Planet. Sci. Lett.* **2009**, *278*, 350–360. [CrossRef]

26.　Bulanova, G.P. The formation of diamond. *J. Geochem. Explor.* **1995**, *53*, 2–23. [CrossRef]

27.　Wang, A.; Pasteris, J.D.; Meyer, H.O.A.; DeleDuboi, M.L. Magnesite-bearing inclusion assemblage in natural diamond. *Earth Planet. Sci. Lett.* **1996**, *141*, 293–306. [CrossRef]

28.　Navon, O.; Hutcheon, I.D.; Rossman, G.R.; Wasserburg, G.J. Mantle-derived fluids in diamond micro-inclusions. *Nature* **1988**, *335*, 784–789. [CrossRef]

29. Schrauder, M.; Navon, O. Hydrous and carbonatitic mantle fluids in fibrous diamonds from Jwaneng, Botswana. *Geochim. Cosmochim. Acta* **1994**, *58*, 761–771. [CrossRef]

30. Sobolev, N.V.; Kaminsky, F.V.; Griffin, W.L.; Yefimova, E.S.; Win, T.T.; Ryan, C.G.; Botkunov, A.I. Mineral inclusions in diamonds from the Sputnik kimberlite pipe, Yakutia. *Lithos* **1997**, *39*, 135–157. [CrossRef]

31. Izraeli, E.S.; Harris, J.W.; Navon, O. Brine inclusions in diamonds: A new upper mantle fluid. *Earth Planet. Sci. Lett.* **2001**, *187*, 1–10. [CrossRef]

32. Stachel, T.; Harris, J.W.; Brey, G.P. Rare and unusual mineral inclusions in diamonds from Mwadui, Tanzania. *Contrib. Miner. Pet.* **1998**, *132*, 34–47. [CrossRef]

33. Brenker, F.E.; Vollmer, C.; Vincze, L.; Vekemans, B.; Szymanski, A.; Janssens, K.; Szaloki, I.; Nasdala, L.; Joswig, W.; Kaminsky, F. Carbonates from the lower part of transition zone or even the lower mantle. *Earth Planet. Sci. Lett.* **2007**, *260*, 1–9. [CrossRef]

34. Kaminsky, F.; Wirth, R.; Schreiber, B. Carbonatitic inclusions in deep mantle diamond from Juina, Brazil: New minerals in the carbonate-halide association. *Can. Miner.* **2013**, *51*, 669–688. [CrossRef]

35. Bataleva, Y.V.; Novoselov, I.D.; Kruk, A.N.; Furman, O.V.; Reutsky, V.N.; Palyanov, Y.N. Experimental modeling of decarbonation reactions resulting in the formation of Mg, Fe-garnets and $CO_2$-fluid under mantle P,T-parameters. *Russ. Geol. Geophys.* **2020**, *61*, 650–662.

36. Cerantola, V.; Bykova, E.; Kupenko, I.; Merlini, M.; Ismailova, L.; McCammon, C.; Bykov, M.; Chumakov, A.I.; Petitgirard, S.; Kantor, I.; et al. Stability of iron-bearing carbonates in the deep Earth's interior. *Nat. Commun.* **2017**, *8*, 15960. [CrossRef]

37. Cerantola, V.; Wilke, M.; Kantor, I.; Ismailova, L.; Kupenko, I.; McCammon, C.; Pascarelli, S.; Dubrovinsky, L.S. Experimental investigation of $FeCO_3$ (siderite) stability in Earth's lower mantle using XANES spectroscopy. *Am. Miner.* **2019**, *104*, 1083–1091. [CrossRef]

38. Tao, R.; Fei, Y.; Zhang, L. Experimental determination of siderite stability at high pressure. *Am. Min.* **2013**, *98*, 1565–1572. [CrossRef]

39. Kang, N.; Schmidt, M.W.; Poli, S.; Franzolin, E.; Connolly, J.A.D. Melting of siderite to 20 GPa and thermodynamic properties of $FeCO_3$-melt. *Chem. Geol.* **2015**, *400*, 34–43. [CrossRef]

40. Liu, J.; Lin, J.-F.; Prakapenka, V.B. High-pressure orthorhombic ferromagnesite as a potential deep-mantle carbon carrier. *Sci. Rep.* **2015**, *5*, 7640. [CrossRef]

41. Bayarjargal, L.; Fruhner, C.-J.; Schrodt, N.; Winkler, B. $CaCO_3$ phase diagram studied with Raman spectroscopy at pressures up to 50 GPa and high temperatures and DFT modeling. *Phys. Earth Planet. Inter.* **2018**, *281*, 31–45. [CrossRef]

42. Gavryushkin, P.N.; Martirosyan, N.S.; Inerbaev, T.M.; Popov, Z.I.; Rashchenko, S.V.; Likhacheva, A.Y.; Lobanov, S.S.; Goncharov, A.F.; Prakapenka, V.B.; Litasov, K.D. Aragonite-II and $CaCO_3$-VII: New high-pressure, high-temperature polymorphs of $CaCO_3$. *Cryst. Growth Des.* **2017**, *17*, 6291–6296. [CrossRef]

43. Solopova, N.A.; Dubrovinsky, L.; Spivak, A.V.; Litvin, Y.A.; Dubrovinskaia, N. Melting and decomposition of $MgCO_3$ at pressures up to 84 GPa. *Phys. Chem. Miner.* **2015**, *42*, 73–81. [CrossRef]

44. Katsura, T.; Ito, E. Melting and subsolidus phase relations in the $MgSiO_3$–$MgCO_3$ system at high pressures: Implications to evolution of the Earth's atmosphere. *Earth Planet. Sci. Lett.* **1990**, *99*, 110–117. [CrossRef]

45. Fiquet, G.; Guyot, F.; Kunz, M.; Matas, J.; Andrault, D.; Hanfland, M. Structural refinements of magnesite at very high pressure. *Am. Miner.* **2002**, *87*, 1261–1265. [CrossRef]

46. Suito, K.; Namba, J.; Horikawa, T.; Taniguchi, Y.; Sakurai, N.; Kobayashi, M.; Onodera, A.; Shimomura, O.; Kikegawa, T. Phase relations of $CaCO_3$ at high pressure and high temperature. *Am. Miner.* **2001**, *86*, 997–1002. [CrossRef]

47. Li, Z.; Li, J.; Lange, R.; Liu, J.; Militzer, B. Determination of calcium carbonate and sodium carbonate melting curves up to Earth's transition zone pressures with implications for the deep carbon cycle. *Earth Planet. Sci. Lett.* **2017**, *457*, 395–402. [CrossRef]

48. Kennedy, C.S.; Kennedy, G.C. The equilibrium boundary between graphite and diamond. *J. Geophys. Res.* **1976**, *81*, 2467–2470. [CrossRef]

49. Palyanov, Y.N.; Borzdov, Y.M.; Khokhryakov, A.F.; Kupriyanov, I.N.; Sokol, A.G. Effect of nitrogen impurity on diamond crystal growth processes. *Cryst. Growth Des.* **2010**, *10*, 3169–3175. [CrossRef]

50. Palyanov, Y.N.; Sokol, A.G. The effect of composition of mantle fluids/melts on diamond formation processes. *Lithos* **2009**, *112S*, 690–700. [CrossRef]

51. Sokol, A.G.; Khokhryakov, A.F.; Palyanov, Y.N. Composition of primary kimberlite magma: Constraints from melting and diamond dissolution experiments. *Contrib. Miner. Pet.* **2015**, *170*, 26. [CrossRef]

52. Sokol, A.G.; Borzdov, Y.M.; Palyanov, Y.N.; Khokhryakov, A.F. High-temperature calibration of a multi-anvil high pressure apparatus. *High Press. Res.* **2015**, *35*, 139–147. [CrossRef]

53. Bataleva, Y.V.; Palyanov, Y.N.; Sokol, A.G.; Borzdov, Y.M.; Palyanova, G.A. Conditions for the origin of oxidized carbonate-silicate melts: Implications for mantle metasomatism and diamond formation. *Lithos* **2012**, *128*, 113–125. [CrossRef]

54. Palyanov, Y.N.; Bataleva, Y.V.; Sokol, A.G.; Borzdov, Y.M.; Kupriyanov, I.N.; Reutsky, V.N.; Sobolev, N.V. Mantle–slab interaction and redox mechanism of diamond formation. *Proc. Natl. Acad. Sci. USA* **2013**, *110*, 20408–20413. [CrossRef] [PubMed]

55. Bataleva, Y.V.; Palyanov, Y.N.; Sokol, A.G.; Borzdov, Y.M.; Bayukov, O.A. The role of rocks saturated with metallic iron in the formation of ferric carbonate–silicate melts: Experimental modeling under PT-conditions of lithospheric mantle. *Russ. Geol. Geophys.* **2015**, *56*, 143–154. [CrossRef]

56. Boettcher, A.L.; Mysen, B.O.; Allen, J.C. Techniques for the control of water fugacity and oxygen fugacity for experimentation in solid-media high-pressure apparatus. *J. Geophys. Res.* **1973**, *80*, 5898–5901. [CrossRef]

57. Luth, R.W. Natural versus experimental control of oxidation state: Effects on the composition and speciation of C-O-H fluids. *Am. Miner.* **1989**, *74*, 50–57.

58. Berman, R.G. Thermobarometry using multiequilibrium calculations: A new technique with petrologic applications. *Can. Miner.* **1991**, *29*, 833–855.

59. Ogasawara, Y.; Liou, J.G.; Zhang, R.Y. Thermochemical calculation of log$f$O$_2$-T-P stability relations of diamond-bearing assemblages in the model system CaO-MgO-SiO$_2$-CO$_2$-H$_2$O. *Russ. Geol. Geophys.* **1997**, *2*, 587–598.

60. Robie, R.A.; Hemingway, B.S.; Fischer, J.R. *Geological Survey Bulletin 1452*; United States Government, Printing Office: Washington, DC, USA, 1978.

61. Holland, T.J.B.; Powell, L. An enlarged and updated internally consistent thermodynamic dataset with uncertainties and correlations: K$_2$O–Na$_2$O–CaO–MgO–FeO–Fe$_2$O$_3$–Al$_2$O$_3$–TiO$_2$–SiO$_2$–C–H$_2$–O$_2$. *J. Metamorph. Geol.* **1990**, *8*, 89–124. [CrossRef]

62. Wendlandt, R.F.; Huebner, S.J.; Harrison, W.J. The redox potential of boron nitride and implications for its use as a crucible material in experimental petrology. *Am. Miner.* **1982**, *67*, 170–174.

63. Farokhpoor, R.; Bjørkvik, B.J.A.; Lindeberg, E.; Torsæter, O. CO$_2$ Wettability Behavior During CO$_2$ Sequestration in Saline Aquifer -An Experimental Study on Minerals Representing Sandstone and Carbonate. *Energy Procedia.* **2013**, *37*, 5339–5351. [CrossRef]

64. Chiquet, P.; Broseta, D.; Thibeau, S. Wettability alteration of caprock minerals by carbon dioxide. *Geofluids* **2007**, *7*, 112–122. [CrossRef]

65. McCandless, T.E.; Gurney, J.J. Sodium in garnet and potassium in clinopyroxene: Criteria for classifying mantle eclogites. In *Kimberlites and Related Rocks, Vol. 2. Their Mantle/Crust Setting, Diamonds and Diamond Exploration*; Ross, J., Ed.; Geological Society of Australia, Special Publications: Melbourne, Australia, 1989; Volume 14, pp. 827–832.

66. Bulanova, G.P.; Walter, M.J.; Smith, C.B.; Kohn, S.C.; Armstrong, L.S.; Blundy, J.; Gobbo, L. Mineral inclusions in sublithospheric diamonds from Collier 4 kimberlite pipe, Juina, Brazil: Subducted protoliths, carbonated melts and primary kimberlite magmatism. *Contrib. Miner. Pet.* **2010**, *160*, 489–510. [CrossRef]

67. Stachel, T.; Harris, J.W.; Brey, G.P.; Joswig, W. Kankan diamonds (Guinea) II: Lower mantle inclusion parageneses. *Contrib. Miner. Pet.* **2000**, *140*, 16–27. [CrossRef]

68. Walmsley, J.C.; Lang, A.R. On sub-micrometre inclusions in diamond coat: Crystallography and composition of ankerites and related rhombohedral carbonates. *Miner. Mag.* **1992**, *56*, 533–543. [CrossRef]

69. Skuzovatov, S.Y.; Zedgenizov, D.A.; Ragozin, A.L.; Shatsky, V.S. Growth medium composition of coated diamonds from the Sytykanskaya kimberlite pipe (Yakutia). *Russ. Geol. Geophys.* **2012**, *53*, 1197–1208. [CrossRef]

70. Aulbach, S.; Viljoen, K.S.; Gerdes, A. Diamondiferous and barren eclogites and pyroxenites from the western Kaapvaal craton record subduction processes and mantle metasomatism, respectively. *Lithos* **2020**, *368–369*, 105588. [CrossRef]

71. Palyanov, Y.N.; Sokol, A.G.; Khokhryakov, A.F.; Kruk, A.N. Conditions of diamond crystallization in kimberlite melt: Experimental data. *Russ. Geol. Geophys.* **2015**, *56*, 196–210. [CrossRef]

72. Pal'yanov, Y.N.; Sokol, A.G.; Khokhryakov, A.F.; Pal'yanova, G.A.; Borzdov, Y.M.; Sobolev, N.V. Diamond and graphite crystallization in COH fluid at PT parameters of the natural diamond formation. *Dokl. Earth Sci.* **2000**, *375*, 1395–1398.

73. Palyanov, Y.N.; Shatsky, V.S.; Sokol, A.G.; Tomilenko, A.A.; Sobolev, N.V. Crystallization of metamorphic diamond: An experimental modeling. *Dokl. Earth Sci.* **2001**, *381*, 935–938.